Estimation of Subpixel Target Size for Remotely Sensed Imagery

Chein-I Chang, *Senior Member, IEEE*, Hsuan Ren, Chein-Chi Chang, Francis D'Amico, and James O. Jensen

***Abstract*—One of the challenges in remote sensing image processing is subpixel detection where the target size is smaller than the ground sampling distance, therefore, embedded in a single pixel. Under such a circumstance, these targets can be only detected spectrally at the subpixel level, not spatially as ordinarily conducted by classical image processing techniques. This paper investigates a more challenging issue than subpixel detection, which is the estimation of target size at the subpixel level. More specifically, when a subpixel target is detected, we would like to know "what is the size of this particular target within the pixel?" The proposed approach is to estimate the abundance fraction of a subpixel target present in a pixel, then find what portion it contributes to the pixel that can be used to determine the size of the subpixel target by multiplying the ground sampling distance. In order to make our idea work, the subpixel target abundance fraction must be accurately estimated to truly reflect the portion of a subpixel target occupied within a pixel. So, a fully constrained linear unmixing method is required to reliably estimate the abundance fractions of a subpixel target for its size estimation. In this paper, a recently developed fully constrained least squares linear unmixing is used for this purpose. Experiments are conducted to demonstrate the utility of the proposed method in comparison with an unconstrained linear unmixing method, unconstrained least squares method, two partially constrained least square linear unmixing methods, sum-to-one constrained least squares, and nonnegativity constrained least squares.**

***Index Terms*—Fully constrained least squares (FCLS), fully constrained least squares linear unmixing (FCLSLU), nonnegativity constrained least squares (NCLS), sum-to-one constrained least squares (SCLS), unconstrained least squares (ULS), unsupervised fully constrained least squares linear unmixing (UFCLSLU).**

I. Introduction

ONE OF THE advantages of using hyperspectral imaging is subpixel detection, which detects targets at the subpixel scale. In many applications, targets of interest may occur with low probabilities or may have relatively small size, such as special species in agriculture and ecology, rare minerals in geology, vehicles in a large battlefield, etc. Under these circumstances, spatial-based image processing techniques may not be effective to extract these targets, particularly when the size of targets is smaller than the pixel resolution (i.e., ground sampling distance). Such targets are generally embedded in a single pixel vector and are referred to as subpixel targets. In this case, spatial-analysis-based techniques are unlikely to find these subpixel targets, and we must rely on techniques that can extract their spectral characteristics. One commonly used method is linear unmixing (LU) [1]–[3], which models an image pixel vector as a linear mixture of a finite number of image endmembers assumed to be present in the image data, then unmixes the pixel vector by finding their corresponding abundance fractions.

In this paper, we investigate an interesting issue associated with subpixel detection. If a subpixel target is detected within a single pixel vector, what is its size? In order to address this problem, we develop an approach that enables us to reliably estimate the abundance fraction of a subpixel target, then multiply the obtained abundance fraction by the ground sampling distance to calculate its size. Such an approach is effective only if the true abundance fraction of a subpixel target contained in a pixel vector is estimated accurately. A fully constrained least squares linear unmixing (FCLSLU), which was recently developed for material quantification in [4], seems to provide a reasonable solution where two constraints, abundance sum-to-one constraint (ASC) and abundance nonnegativity constraint (ANC), are imposed on abundance fractions of image endmembers used in a linear mixture model. It implements the ANC and the ASC in the least squares sense to derive fully constrained least squares (FCLS) solutions that can be further used to estimate the size of a subpixel target. In order to make the FCLSLU work in an unknown environment, an automatic target detection and classification algorithm (ATDCA) developed in [5]–[7] is further incorporated into the FCLSLU to make it an unsupervised FCLSLU (UFCLSLU), with the ability to detect subpixel targets without prior knowledge. Finally, computer simulations and real hyperspectral image experiments are conducted to substantiate the proposed UFCLSLU in estimating the size of a subpixel target where an unconstrained least squares (ULS) linear unmixing and two partially constrained least squares linear unmixing methods [6], sum-to-one constrained least squares (SCLS) linear unmixing and nonnegativity constrained least squares (NCLS) linear unmixing, are also included for comparative analysis.

This paper is organized as follows. Section II briefly reviews unconstrained and constrained least-squares-based linear unmixing methods. Section III describes the ATDCA in detail. Section IV derives an unsupervised FCLSLU that implements the FCLSLU in conjunction with the ATDCA. Section V presents experiments that validate the utility of the UFCLSLU in subpixel target size estimation. Section V draws some conclusions.

Manuscript received June 7, 2003; revised January 10, 2004. This work was supported in part by the National Research Council under a Senior Research Associateship and in part by the U.S. Army Edgewood Chemical and Biological Center under a Postdoctoral Associateship.

C.-I Chang is with the Remote Sensing Signal and Image Processing Laboratory, Department of Computer Science and Electrical Engineering, University of Maryland Baltimore County, Baltimore, MD 21250 USA.

H. Ren is with the Center for Space and Remote Sense Research, Department of Information Engineering, National Central University, Chungli, Taiwan, R.O.C.

C.-C. Chang is with the Department of Civil and Environmental Engineering, University of Maryland Baltimore County, Baltimore, MD 21250 USA.

F. D'Amico and J. O. Jensen are with the U.S. Army Edgewood Chemical and Biological Center, Aberdeen Proving Ground, MD 21010 USA.

Digital Object Identifier 10.1109/TGRS.2004.826559

0196-2892/04$20.00 © 2004 IEEE

II. Least-Sqaures-Based Linear Unmixing

Let $\mathbf{r}$ be an $L \times 1$ column image pixel vector in a multispectral or hyperspectral image where L is the number of spectral bands. Assume that $\mathbf{M}$ is an $L \times p$ signature matrix denoted by $\mathbf{M} = \lfloor \mathbf{m}_1 \mathbf{m}_2 \cdots \mathbf{m}_p \rfloor$ where $\mathbf{m}_j$ is an $L \times 1$ column vector represented by the jth image endmember signature resident in the pixel vector $\mathbf{r}$, and p is the number of signatures of interest. Let $\boldsymbol{\alpha} = (\alpha_1, \alpha_2, \ldots \alpha_p)^T$ be a $p \times 1$ abundance column vector associated with $\mathbf{r}$ where α_j denotes the fraction of the jth signature in the pixel vector $\mathbf{r}$. A linear mixture model assumes that the spectral signature of a pixel vector $\mathbf{r}$ is linearly superimposed by spectral signatures of image endmembers $\mathbf{m}_1, \mathbf{m}_2, \ldots, \mathbf{m}_p$ present in the pixel vector $\mathbf{r}$ and can be described by

$$\mathbf{r} = \mathbf{M}\boldsymbol{\alpha} + \mathbf{n} \tag{1}$$

where $\mathbf{n}$ is an $L \times 1$ column additive noise vector representing a measurement or model error. Equation (1) is a general linear mixture model with no constraints imposed on the abundance vector $\boldsymbol{\alpha} = (\alpha_1, \alpha_2, \ldots \alpha_p)^T$ and can be solved by interpreting the noise $\mathbf{n}$ as the error $\mathbf{e}$ resulting from the goodness of fit in the least squares sense and then minimizing its least squares error. To solve a constrained problem, an unconstrained least squares solution to (1) is first found, then further used as a base to develop iterative algorithms to solve for constrained least squares mixing problems. Once a fully constrained least square estimate $\hat{\boldsymbol{\alpha}}$ is solved for the abundance vector $\boldsymbol{\alpha}$, the target size can be estimated by multiplying the estimated abundance fractions $\hat{\boldsymbol{\alpha}}$ by the ground sampling distance.

A. ULS Linear Unmixing

In order to estimate $\boldsymbol{\alpha} = (\alpha_1 \alpha_2, \ldots, \alpha_p)^T$ from (1), several techniques have been developed and studied in [6], [8], and [9].

Using the least squares error as an optimal criterion for (1), the unconstrained optimal least squares estimate of $\boldsymbol{\alpha}, \hat{\boldsymbol{\alpha}}_{\mathrm{ULS}}$ can be found by minimizing the following least square error function:

$$E(\boldsymbol{\alpha}) = \mathbf{n}^T\mathbf{n} = (\mathbf{r} - \mathbf{M}\boldsymbol{\alpha})^T(\mathbf{r} - \mathbf{M}\boldsymbol{\alpha}). \tag{2}$$

Differentiating $E[\boldsymbol{\alpha}]$ in (2) with respect to $\boldsymbol{\alpha}$ and setting to zero yields

$$\left.\frac{\partial E(\boldsymbol{\alpha})}{\partial \boldsymbol{\alpha}}\right|_{\hat{\boldsymbol{\alpha}}_{\mathrm{ULS}}} = 0 \Rightarrow -2\mathbf{M}^T\mathbf{r} + 2(\mathbf{M}^T\mathbf{M})\hat{\boldsymbol{\alpha}}_{\mathrm{ULS}} = 0 \tag{3}$$

and

$$\hat{\boldsymbol{\alpha}}_{\mathrm{ULS}} = (\mathbf{M}^T\mathbf{M})^{-1}\mathbf{M}^T\mathbf{r} \tag{4}$$

where $\hat{\boldsymbol{\alpha}}_{\mathrm{ULS}}$ is a function of the image pixel vector $\mathbf{r}$. For simplicity, the dependency of $\hat{\boldsymbol{\alpha}}_{\mathrm{ULS}}$ on $\mathbf{r}$ is not included in the notation.

B. SCLS Linear Unmixing

The $\hat{\boldsymbol{\alpha}}_{\mathrm{ULS}}$ specified by (4) was obtained by imposing no constraints on the abundance vector $\boldsymbol{\alpha}$. In order to find the fully constrained optimal least squares estimate of $\boldsymbol{\alpha}$, we first consider the SCLS linear mixing problem [3], [4], [6], [9], which can be described as follows:

$$\min_{\boldsymbol{\alpha}}\{(\mathbf{r} - \mathbf{M}\boldsymbol{\alpha})^T(\mathbf{r} - \mathbf{M}\boldsymbol{\alpha})\}$$

subject to

$$\sum_{j=1}^{p} \alpha_j = 1 \quad \text{or} \quad \mathbf{1}^T\boldsymbol{\alpha} = 1 \tag{5}$$

where $\mathbf{1}^T = \underbrace{(1, 1, \ldots, 1)}_{p}$ is a unity vector with all elements equal to one.

Let ξ be the Lagrange multiplier and $J(\boldsymbol{\alpha})$ be the Lagrangian given by

$$J(\boldsymbol{\alpha}) = \frac{1}{2}(\mathbf{r} - \mathbf{M}\boldsymbol{\alpha})(\mathbf{r} - \mathbf{M}\boldsymbol{\alpha})^T - \xi(\mathbf{1}^T\boldsymbol{\alpha} - 1). \tag{6}$$

Differentiating $J(\boldsymbol{\alpha})$ in (6) with respect to $\boldsymbol{\alpha}$ and setting to zero yields

$$\begin{aligned}\left.\frac{\partial J(\boldsymbol{\alpha})}{\partial \boldsymbol{\alpha}}\right|_{\hat{\boldsymbol{\alpha}}_{\mathrm{SCLS}}} = 0 &\Rightarrow -\mathbf{M}^T\mathbf{M}\hat{\boldsymbol{\alpha}}_{\mathrm{SCLS}} = \mathbf{M}^T\mathbf{r} + \xi\mathbf{1} \\ &\Rightarrow \hat{\boldsymbol{\alpha}}_{\mathrm{SCLS}} = (\mathbf{M}^T\mathbf{M})^{-1}\mathbf{M}^T\mathbf{r} + (\mathbf{M}^T\mathbf{M})^{-1}\xi\mathbf{1} \\ &\Rightarrow \hat{\boldsymbol{\alpha}}_{\mathrm{SCLS}} = \hat{\boldsymbol{\alpha}}_{\mathrm{ULS}} + (\mathbf{M}^T\mathbf{M})^{-1}\xi\mathbf{1}\end{aligned} \tag{7}$$

where the optimal solution to (5) is denoted by $\hat{\boldsymbol{\alpha}}_{\mathrm{SCLS}}$, and $\hat{\boldsymbol{\alpha}}_{\mathrm{ULS}}$ is the unconstrained least squares estimate of $\boldsymbol{\alpha}$ given by (4).

Equation (7) shows that $\hat{\boldsymbol{\alpha}}_{\mathrm{SCLS}}$ is the unconstrained least squares estimate $\hat{\boldsymbol{\alpha}}_{\mathrm{ULS}}$ given by (5) plus a correction term $(\mathbf{M}^T\mathbf{M})^{-1}\xi\mathbf{1}$ resulting from the constraint $\sum_{j=1}^{p} \alpha_j = 1$. In order to solve the Lagrange multiplier ξ in (7), we substitute (7) into the constraint $\sum_{j=1}^{p} \alpha_j = 1$ and obtain

$$\begin{aligned}1 = \mathbf{1}^T\hat{\boldsymbol{\alpha}}_{\mathrm{SCLS}} &= \mathbf{1}^T\hat{\boldsymbol{\alpha}}_{\mathrm{ULS}} + \mathbf{1}^T(\mathbf{M}^T\mathbf{M})^{-1}\xi\mathbf{1} \Rightarrow \xi \\ &= [\mathbf{1}^T(\mathbf{M}^T\mathbf{M})^{-1}\mathbf{1}]^{-1}(\mathbf{1} - \mathbf{1}^T\hat{\boldsymbol{\alpha}}_{\mathrm{ULS}})\end{aligned} \tag{8}$$

which results in the following closed-from solution to (5):

$$\begin{aligned}\hat{\boldsymbol{\alpha}}_{\mathrm{SCLS}} = \hat{\boldsymbol{\alpha}}_{\mathrm{ULS}} &+ (\mathbf{M}^T\mathbf{M})^{-1}\mathbf{1} \\ &\cdot [\mathbf{1}^T(\mathbf{M}^T\mathbf{M})^{-1}\mathbf{1}]^{-1}(\mathbf{1} - \mathbf{1}^T \times \hat{\boldsymbol{\alpha}}_{\mathrm{ULS}}).\end{aligned} \tag{9}$$

C. FCLSLU

Since the SCLS solution derived in (9) is only based on the constraint $\sum_{j=1}^{p} \alpha_j = 1$, it does not guarantee that the estimated abundance fractions are nonnegative, i.e., $\alpha_j \geq 0$ for all $1 \leq j \leq p$. In this section, the ANC is imposed as an additional constraint on (1), which results in a fully constrained least squares (FCLS) problem

$$\text{Minimize LSE} = (\mathbf{M}\boldsymbol{\alpha} - \mathbf{r})^T(\mathbf{M}\boldsymbol{\alpha} - \mathbf{r})$$

subject to

$$\boldsymbol{\alpha} \geq 0 \text{ and } \sum_{j=1}^{p} \alpha_j = 1 \tag{10}$$

where $\boldsymbol{\alpha} \geq 0$ represents the nonnegativity constraint: $\alpha_j \geq 0$ for all $1 \leq j \leq p$. Since $\boldsymbol{\alpha} \geq 0$ is a set of p inequalities, there is no analytic form similar to the SCLS solution that can be derived to find the optimal solution. To circumvent this dilemma, we first consider the NCLS problem, which only imposes the ANC on (1), i.e.,

$$\text{Minimize LSE} = (\mathbf{M}\boldsymbol{\alpha} - \mathbf{r})^T(\mathbf{M}\boldsymbol{\alpha} - \mathbf{r}) \text{ subject to } \alpha \geq 0 \tag{11}$$

then find the FCLS solution to (10) by solving the NCLS problem specified by (11) in conjunction with the SCLS solution obtained by (9).

First of all, we introduce an unknown p-dimensional positive constraint constant vector $\mathbf{c} = [c_1 c_2 \dots c_p]^T$ with $c_j > 0$ for $\mathbf{1} \le j \le p$ to take care of the nonnegativity constraint and a Lagrange multiplier vector $\boldsymbol{\lambda} = (\lambda_1, \lambda_2, \dots, \lambda_p)^T$. Through the vector $\mathbf{c}$, we form a Lagrangian J as follows:

$$J(\boldsymbol{\alpha}) = \frac{1}{2}(\mathbf{M}\boldsymbol{\alpha} - \mathbf{r})^T(\mathbf{M}\boldsymbol{\alpha} - \mathbf{r}) + \boldsymbol{\lambda}(\boldsymbol{\alpha} - \mathbf{c}) \tag{12}$$

with the constraint given by $\boldsymbol{\alpha} = \mathbf{c}$. Differentiating $J(\boldsymbol{\alpha})$ with respect to $\boldsymbol{\alpha}$

$$\left.\frac{\partial J(\boldsymbol{\alpha})}{\partial \boldsymbol{\alpha}}\right|_{\hat{\boldsymbol{\alpha}}_{\mathrm{NCLS}}} = 0 \Rightarrow \mathbf{M}^T\mathbf{M}\hat{\boldsymbol{\alpha}}_{\mathrm{NCLS}} - \mathbf{M}^T\mathbf{r} + \boldsymbol{\lambda} = 0 \tag{13}$$

results in the following two iterative equations:

$$\begin{aligned}\hat{\boldsymbol{\alpha}}_{\mathrm{NCLS}} &= (\mathbf{M}^T\mathbf{M})^{-1}\mathbf{M}^T\mathbf{r} - (\mathbf{M}^T\mathbf{M})^{-1}\boldsymbol{\lambda} \\ &= \hat{\boldsymbol{\alpha}}_{\mathrm{ULS}} - (\mathbf{M}^T\mathbf{M})^{-1}\boldsymbol{\lambda}\end{aligned} \tag{14}$$

and

$$\boldsymbol{\lambda} = \mathbf{M}^T(\mathbf{r} - \mathbf{M}\hat{\boldsymbol{\alpha}}_{\mathrm{NCLS}}). \tag{15}$$

By iterating (14) and (15), we can solve the optimal NCLS solution $\hat{\boldsymbol{\alpha}}_{\mathrm{NCLS}}$.

In order to solve the FCLS problem [i.e., (10)], we include the ASC in the signature matrix $\mathbf{M}$ by introducing a new signature matrix $\mathbf{N}$ defined by

$$\mathbf{N} = \begin{bmatrix} \delta\mathbf{M} \\ \mathbf{1}^T \end{bmatrix} \tag{16}$$

with $\mathbf{1}^T = (\underbrace{11\dots1}_{p})$, and a vector $\mathbf{s}$ denoted by

$$\mathbf{s} = \begin{bmatrix} \delta\mathbf{r} \\ \mathbf{1} \end{bmatrix}. \tag{17}$$

The parameter δ in (16) and (17) is included to control the impact of the ASC on the FCLS solution. In our experiments, the value of δ was set to 10^{-6}. With these two equations, the FCLS solution can be derived directly from the NCLS solution by replacing $\mathbf{M}$ and $\mathbf{r}$ used in the NCLS solution with $\mathbf{N}$ and $\mathbf{s}$. An algorithm of finding the FCLS solution, referred to as fully constrained least squares linear unmixing (FCLSLU), can be summarized as follows.

FCLSLU Algorithm:

1) Specify values of the parameter δ (10^{-6} in our experiments) and the error tolerance ε.
2) Use (4) to generate an unconstrained least squares solution $\hat{\boldsymbol{\alpha}}_{\mathrm{ULS}}$.
3) Iterate (14) and (15) with $\mathbf{M}$ and $\mathbf{r}$ replaced by $\mathbf{N}$ and $\mathbf{s}$ defined in (16) and (17), respectively, until the algorithm converges within ε.

III. ATDCA

When the FCLSLU is implemented, it requires complete knowledge about the signature matrix $\mathbf{M}$. In reality, obtaining such prior knowledge is difficult, if not impossible. So, in this section, we describe an unsupervised method, called the automatic target detection and classification algorithm, that can be used to generate target signatures to form the $\mathbf{M}$. The ATDCA comprises two processes: automatic target generation process (ATGP) followed by target classification process (TCP), both of which make use of an orthogonal subspace projector defined in [5]–[7] by

$$P_{\mathbf{U}}^{\perp} = \mathbf{I} - \mathbf{U}(\mathbf{U}^T\mathbf{U})^{-1}\mathbf{U}^T. \tag{18}$$

It should be noted that the desired signature matrix $\mathbf{M}$ is constructed by including all target signatures found by the ATGP and then is used for target classification in the TCP.

Assume that $\mathbf{t}_0$ is an initial target signature. The ATGP begins with the initial target signature $\mathbf{t}_0$ by applying an orthogonal subspace projector $P_{\mathbf{t}}^{\perp}$ specified by (18) with $\mathbf{U} = \mathbf{t}$ to all image pixel vectors. It then finds a target signature, denoted by $\mathbf{t}_1$ with the maximum projection in the orthogonal complement space, denoted by $\langle \mathbf{t}_0 \rangle^{\perp}$ that is orthogonal to the space, $\langle \mathbf{t}_0 \rangle$ linearly spanned by $\mathbf{t}_0$. The reason for this selection is that the selected $\mathbf{t}_1$ generally has the most distinct features from $\mathbf{t}_0$ in the sense of orthogonal projection because $\mathbf{t}_1$ has the largest magnitude of the projection in $\langle \mathbf{t}_0 \rangle^{\perp}$ produced by $P_{\mathbf{t}_0}^{\perp}$. A second target signature $\mathbf{t}_2$ can be found by applying an orthogonal subspace projector $P_{[\mathbf{t}_0\mathbf{t}_1]}^{\perp}$ with $\mathbf{U} = [\mathbf{t}_0\mathbf{t}_1]$ to the original image, and a target signature that has the maximum projection in $\langle \mathbf{t}_0, \mathbf{t}_1 \rangle^{\perp}$ is selected as $\mathbf{t}_2$. The above procedure is repeated over and over again to find a third target signature $\mathbf{t}_3$, a fourth target signature $\mathbf{t}_4$, etc. In order to terminate the ATGP, a stopping rule is required. If we let $\mathbf{U}_i = [\mathbf{t}_1\mathbf{t}_2 \dots \mathbf{t}_i]$ be the ith target signature matrix generated at the ith stage, we define an orthogonal projection correlation index (OPCI) by

$$\eta_i = \mathbf{t}_0^T P_{\mathbf{U}_i}^{\perp}\mathbf{t}_0 \tag{19}$$

which can be used to measure the similarity between two consecutive generated target signatures. Since $\mathbf{U}_{i-1}$ is a submatrix of $\mathbf{U}_i$, then $\eta_i = \mathbf{t}_0^T P_{\mathbf{U}_i}^{\perp}\mathbf{t}_0 \le \eta_{i-1} = \mathbf{t}_0^T P_{\mathbf{U}_{i-1}}^{\perp}\mathbf{t}_0$ for all i's. This implies that the sequence $\{\mathbf{t}_0^T P_{\mathbf{U}_i}^{\perp}\mathbf{t}_0\}$ is monotonically decreasing at i. In other words, the OPCI sequence $\{\eta_i\}$ is monotonically decreasing at i. Using this property as a stopping criterion, the ATGP can be described as follows.

ATGP:

1) *Initial condition:* Select an initial target signature of interest denoted by $\mathbf{t}_0$. Let ε be the prescribed error threshold.
   Set $i = 0$ and $\mathbf{U}_0 = \phi$.
2) Apply $P_{\mathbf{t}_0}^{\perp}$ via (18) to all image pixel vectors $\mathbf{r}$ in the image.
3) Find the first target signature, denoted by $\mathbf{t}_1$, which has the maximum orthogonal projection

$$\mathbf{t}_1 = \arg\left\{\max_{\mathbf{r}}\left[\left(P_{\mathbf{t}_0}^{\perp}\mathbf{r}\right)^T\left(P_{\mathbf{t}_0}^{\perp}\mathbf{r}\right)\right]\right\}. \tag{20}$$

   Set $i = 1$ and $\mathbf{U}_1 = \mathbf{t}_1$.

4) If $\eta_1 = \mathbf{t}_0^T P_{\mathbf{U}_1}^{\perp} \mathbf{t}_0 < \varepsilon$, go to Step 8). Otherwise, set $i = i + 1$ and continue.
5) Find the ith target $\mathbf{t}_i$ generated at the ith stage by

$$\mathbf{t}_1 = \arg\left\{\max_{\mathbf{r}}\left[\left(P_{[\mathbf{t}_0\mathbf{U}_{i-1}]}^{\perp}\mathbf{r}\right)^T\left(P_{[\mathbf{t}_0\mathbf{U}_{i-1}]}^{\perp}\mathbf{r}\right)\right]\right\} \quad (21)$$

where $\mathbf{U}_{i-1} = [\mathbf{t}_1\mathbf{t}_2\ldots\mathbf{t}_{i-1}]$ is the target signature set generated at the $(i-1)$st stage.
6) Let $\mathbf{U}_i = [\mathbf{t}_1\mathbf{t}_2\ldots\mathbf{t}_i]$ be the ith target signature set, calculate OPCI $\eta_i = \mathbf{t}_0^T P_{\mathbf{U}_i}^{\perp}\mathbf{t}_0$, and compare η_i to a prescribed threshold ε.
7) *Stopping rule:* If $\eta_i > \varepsilon$, go to Step 5). Otherwise continue.
8) At this stage, the ATGP is terminated. At this point, the target set $\mathbf{U}_i$ generated at this point contains i target signatures, which do not include the initial target signature $\mathbf{t}_0$.

After the ATGP is terminated, the ATGP-generated targets are then fed to the TCP for target classification. In order to initialize the ATGP without knowing $\mathbf{t}_0$, we select a target signature with the maximum length as the initial target $\mathbf{t}_0$, namely, $\mathbf{t}_0 = \arg\{\max_{\mathbf{r}}[\mathbf{r}^T\mathbf{r}]\}$, which has the highest intensity, i.e., the brightest pixel in the image scene. It is worth noting that this selection may not be necessarily the best selection. However, according to our experiments, it was found that the brightest pixel was always extracted later on, if it was not used as an initial target pixel in the initialization. A detailed implementation of the ATDCA is given as follows.

ATDCA:

1) Select $\mathbf{t}_0 = \arg\{\max_{\mathbf{r}}[\mathbf{r}^T\mathbf{r}]\}$.
2) Use $\mathbf{t}_0$ as the initial target signature in Step 1) of the ATGP.
3) Follow Steps 2)–8) outlined in the ATGP to generate $\mathbf{U}_i$.
4) Use the TCP to classify $\mathbf{t}_0$ and all the targets in $\mathbf{U}_i$ individually.

The OSP classifier $P_{\mathrm{OSP}} = \mathbf{t}_j^T P_{\mathbf{U}}^{\perp}$ proposed in [10] is the classifier used in the TCP to classify all individual targets $\mathbf{t}_j$ with $\mathbf{U} = [\mathbf{t}_0\mathbf{t}_1\ldots\mathbf{t}_{j-1}\mathbf{t}_{j+1}\ldots\mathbf{t}_i]$. Since there are $i+1$ target signatures (i.e., $\mathbf{t}_0$ and i target signatures $\mathbf{t}_1, \mathbf{t}_2, \ldots, \mathbf{t}_i$ in $\mathbf{U}_i$), $i+1$ images will be generated by the TCP, each of which detects and classifies one particular target.

IV. UFLCSLU

The ATDCA developed in the previous section is an unsupervised process to generate the desired signature matrix $\mathbf{M}$ from the data directly to implement the FCLSLU as an unsupervised FLCSLU. In order to initialize the UFCLSLU, the pixel vector with the maximum length is selected as a desired initial target denoted by $\mathbf{t}_0$. We then assume that all other pixel vectors in the image scene are pure pixels made up of $\mathbf{t}_0$ with 100% abundance. Of course, this is generally not true. So, we find a pixel vector that has the largest LSE from the $\mathbf{t}_0$ and select it as a first target pixel vector denoted by $\mathbf{t}_1$. Because the LSE between $\mathbf{t}_0$ and $\mathbf{t}_1$ is the largest, it can be expected that $\mathbf{t}_1$ is most distinct from $\mathbf{t}_0$. We then form a target signature matrix $\mathbf{M} = [\mathbf{t}_0\mathbf{t}_1]$ and also create the matrix $\mathbf{N}$ and $\mathbf{s}$ using (16) and (17). The FCLSLU algorithm is then used to estimate the abundance fractions for $\mathbf{t}_0$ and $\mathbf{t}_1$, denoted by $\hat{\alpha}_0^{(1)}(\mathbf{r})$ and $\hat{\alpha}_1^{(1)}(\mathbf{r})$ for each pixel vector $\mathbf{r}$, respectively. Here, $\mathbf{r}$ is included in the estimated abundance fractions $\hat{\alpha}_0^{(1)}(\mathbf{r})$ and $\hat{\alpha}_1^{(1)}(\mathbf{r})$ to emphasize that $\hat{\alpha}_0^{(1)}(\mathbf{r})$ and $\hat{\alpha}_1^{(1)}(\mathbf{r})$ are functions of $\mathbf{r}$ and vary with $\mathbf{r}$. The superscript indicates the number of iterations already been executed. Now, we find an optimal constrained linear mixture of $\mathbf{t}_0$ and $\mathbf{t}_1, \hat{\alpha}_0^{(1)}(\mathbf{r})\mathbf{t}_0 + \hat{\alpha}_1^{(1)}(\mathbf{r})\mathbf{t}_1$, to approximate the $\mathbf{r}$. We then calculate the LSE between $\mathbf{r}$ and its estimated linear mixture $\hat{\alpha}_0^{(1)}(\mathbf{r})\mathbf{t}_0 + \hat{\alpha}_1^{(1)}(\mathbf{r})\mathbf{t}_1$ for all image pixel vectors $\mathbf{r}$. Once again, a pixel vector that yields the largest LSE from its estimated linear mixture will be selected to be a second target pixel vector $\mathbf{t}_2$. As expected, such a selected target pixel has the largest projection orthogonal to the space linearly spanned by $\mathbf{t}_0$ and $\mathbf{t}_1$. In other words, the pixel vector that yields the largest LSE resulting from a constrained linear mixture approximation is a most likely target pixel yet to be found in the image scene. The same procedure of using the FCLSLU algorithm with $\mathbf{M} = [\mathbf{t}_0\mathbf{t}_1\mathbf{t}_2]$ is repeated until the resulting LSE is below a prescribed error threshold. If there is partial knowledge available *a priori*, it can be incorporated into the above process. For example, if more than one target signature is known, we can select these target signatures as an initial target set to replace $\mathbf{t}_0$ and then follow the procedure described above until the LSE is sufficiently small. The procedure outlined as above is called unsupervised FCLSLU algorithm, which can be summarized as follows.

Unsupervised FCLSLU Algorithm:

1) *Initial condition:* Select ε to be a prescribed error threshold, and let $\mathbf{t}_0 = \arg\{\max_{\mathbf{r}}[\mathbf{r}^T\mathbf{r}]\}$ where $\mathbf{r}$ is run over all image pixel vectors. Let $k = 0$.
2) Find $\mathbf{t}_1$ that yields the largest $\mathrm{LSE}^{(0)}(\mathbf{r}) = (\mathbf{r}-\mathbf{t}_0)^T(\mathbf{r}-\mathbf{t}_0)$, i.e., $\mathbf{t}_1 = \arg\{\max_{\mathbf{r}} \mathrm{LSE}^{(0)}(\mathbf{r})\}$.
3) Let $k \leftarrow k+1$ and apply the FCLSLU algorithm with the signature matrix $\mathbf{M} = [\mathbf{t}_0\mathbf{t}_1\ldots\mathbf{t}_k], \mathbf{N} = \begin{bmatrix}\delta\mathbf{M} \\ \mathbf{1}^T\end{bmatrix}$, and $\mathbf{s} = \begin{bmatrix}\delta\mathbf{r} \\ \mathbf{1}\end{bmatrix}$ to estimate the abundance fractions of $\mathbf{t}_0, \mathbf{t}_1, \ldots, \mathbf{t}_k, \hat{\alpha}_0^{(k)}(\mathbf{r}), \hat{\alpha}_1^{(k)}(\mathbf{r}), \ldots, \hat{\alpha}_{k-1}^{(k)}(\mathbf{r})$.
4) Find the least squares error defined by

$$\mathrm{LSE}^{(k)}(\mathbf{r}) = \left(\mathbf{r} - \left[\sum_{i-0}^{k}\hat{\alpha}_i^{(k)}(\mathbf{r})\mathbf{t}_i\right]\right)^T\left(\mathbf{r} - \left[\sum_{i-0}^{k}\hat{\alpha}_i^{(k)}(\mathbf{r})\mathbf{t}_i\right]\right) \quad (22)$$

and check the error if $\mathrm{LSE}^{(k)}(\mathbf{r}) < \varepsilon$ for all $\mathbf{r}$. If it is, the algorithm stops. Otherwise continue.
5) Find $\mathbf{t}_{k+1} = \arg\{\max_{\mathbf{r}} \mathrm{LSE}^{(k)}(\mathbf{r})\}$ Go to Step 3).

V. Experimental Results

In this section, computer simulations and real hyperspectral image experiments will be conducted to substantiate and validate our proposed idea.

A. Data to Be Used for Computer Simulations and Image Experiments

The data to be used for experiments are the Hyperspectral Digital Image Collection Experiment (HYDICE) image shown

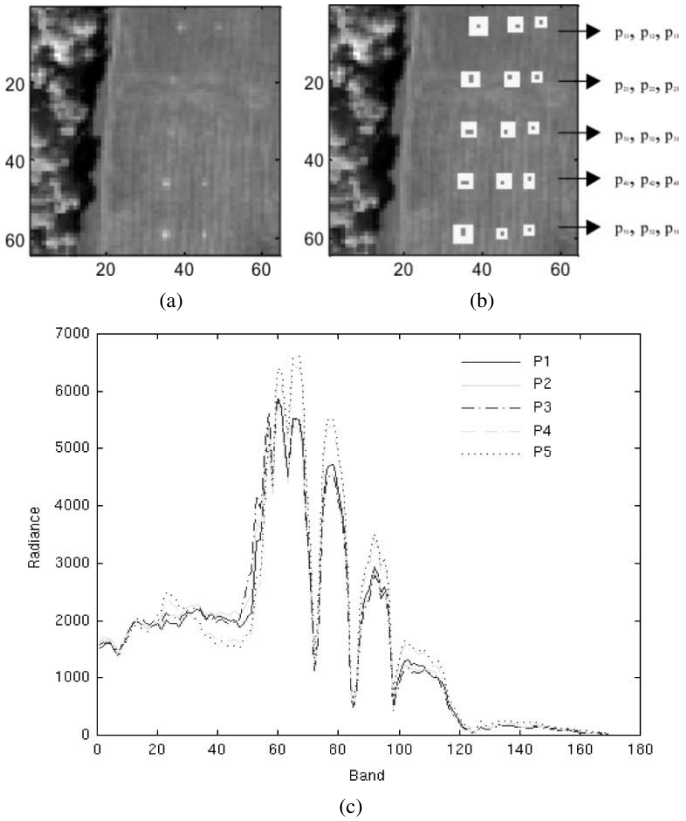

Fig. 1. (a) HYDICE panel scene that contains 15 panels. (b) Ground truth map of spatial locations of the 15 panels. (c) Five panel signatures.

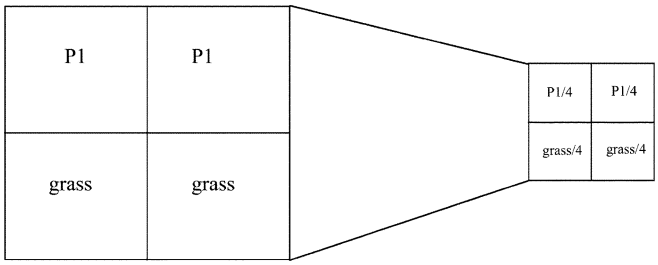

Fig. 2. Simulation of subpixel target pixel P_{12}.

in Fig. 1(a), which has a size of 64×64 pixel vectors with 15 panels in the scene. It was acquired by 210 spectral bands with a spectral coverage from 0.4–2.5 μm. Low-signal/high-noise bands (bands 1–3 and bands 202–210) and water vapor absorption bands (bands 101–112 and bands 137–153) were removed. So, a total of 169 bands were used. The spatial resolution is 1.56 m, and the spectral resolution is 10 nm. Within the scene in Fig. 1(a), there is a large grass field background, a forest on the left edge, and a barely visible road running on the right edge of the scene. There are 15 panels located in the center of the grass field and are arranged in a 5×3 matrix as shown in Fig. 1(b), which provides the ground truth map of Fig. 1(a).

Each element in this matrix is a square panel and is denoted by p_{ij} with rows indexed by i and columns indexed by j. For each row $i = 1, \ldots, 5$, there are three panels $\mathrm{p}_{i1}, \mathrm{p}_{i2}, \mathrm{p}_{i3}$, painted by the same material but with three different sizes. For each column $j = 1, 2, 3$, the five panels $\mathrm{p}_{1j}, \mathrm{p}_{2j}, \mathrm{p}_{3j}, \mathrm{p}_{4j}, \mathrm{p}_{5j}$ have the same size but were painted by five different materials. It should be noted that the panels in rows 2 and 3 are made by

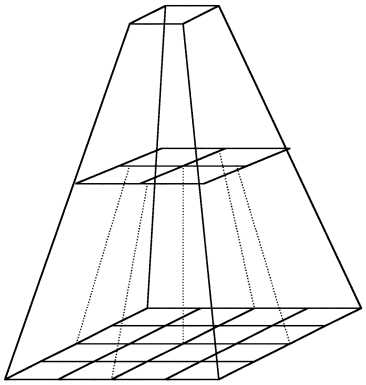

Fig. 3. Illustration of shrinking process by Burt–Adelson's pyramid method.

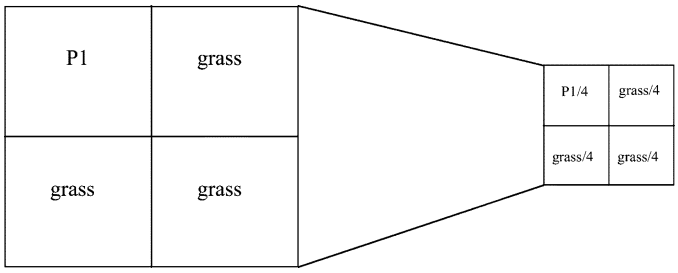

Fig. 4. Simulation of subpixel target pixel P_{13}.

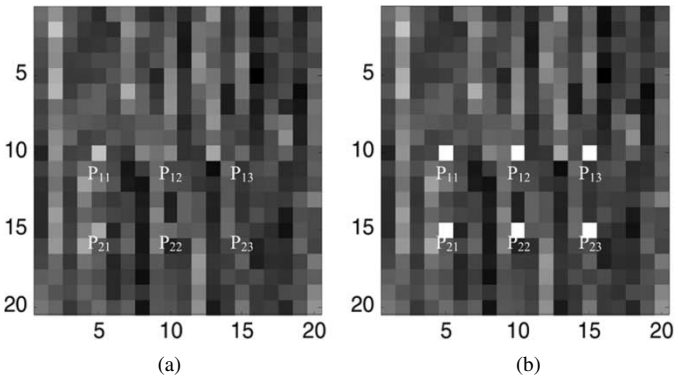

Fig. 5. (a) Simulated image scene. (b) Ground truth map of six implanted panel targets pixels.

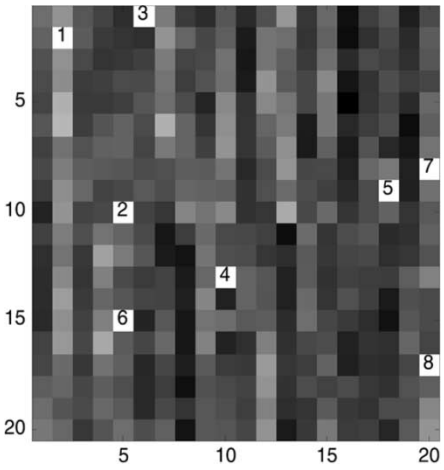

Fig. 6. Eight targets detected by ATDCA in Fig. 4(a).

the same material, but painted by different paints, so are the panels in rows 4 and 5. Nevertheless, they were still considered

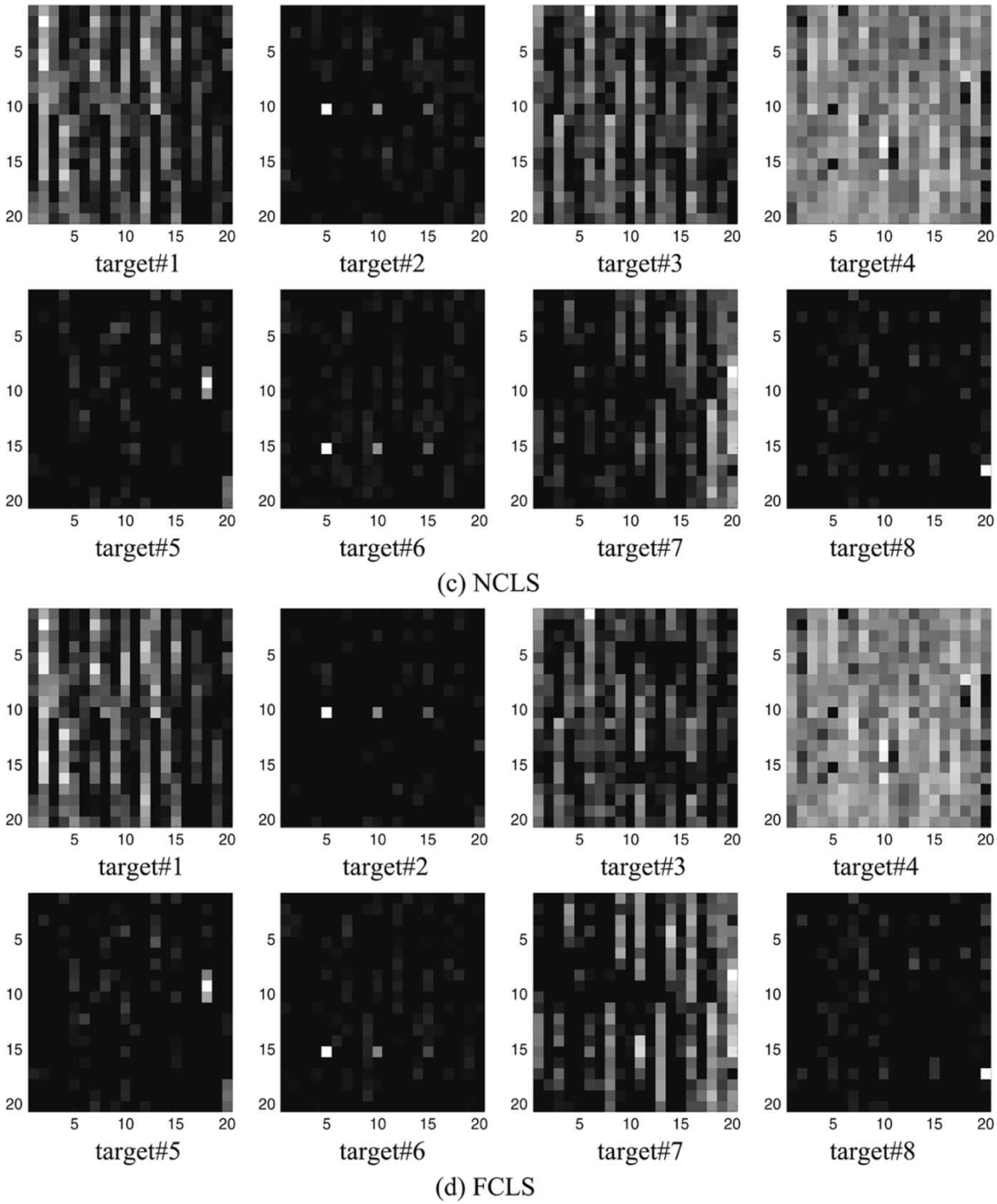

Fig. 7. *(Continued).* Detection results of Fig. 4(a) by (a) ULS, (b) SCLS, (c) NCLS, and (d) FCLS.

as different materials. The sizes of the panels in the first, second, and third columns are 3 m × 3 m, 2 m × 2 m, and 1 m × 1 m, respectively. So, the 15 panels are painted by five different materials and have three different sizes. Since the size of the panels in the third column is 1 m × 1 m, they cannot be seen visually from Fig. 1(a) due to the fact that its size is less than the 1.56-m pixel resolution. Fig. 1(b) shows the precise spatial locations of these 15 panels where red pixels (R pixels) are the panel center pixels, and the pixels in yellow (Y pixels) are panel pixels mixed with the background. The 1.56-m spatial resolution of the image scene suggests that most of the 15 panels are one pixel in size except that $\mathrm{p}_{21}, \mathrm{p}_{31}, \mathrm{p}_{41}, \mathrm{p}_{51}$, which are two-pixel panels.

Fig. 1(c) plots the five panel spectral signatures obtained by averaging R pixels in Fig. 1(b), where the ith panel signature, denoted by Pi, was generated by averaging the red panel center pixels in row i. These panel signatures represent the target knowledge of the panels in each row and will be used for the following computer simulations.

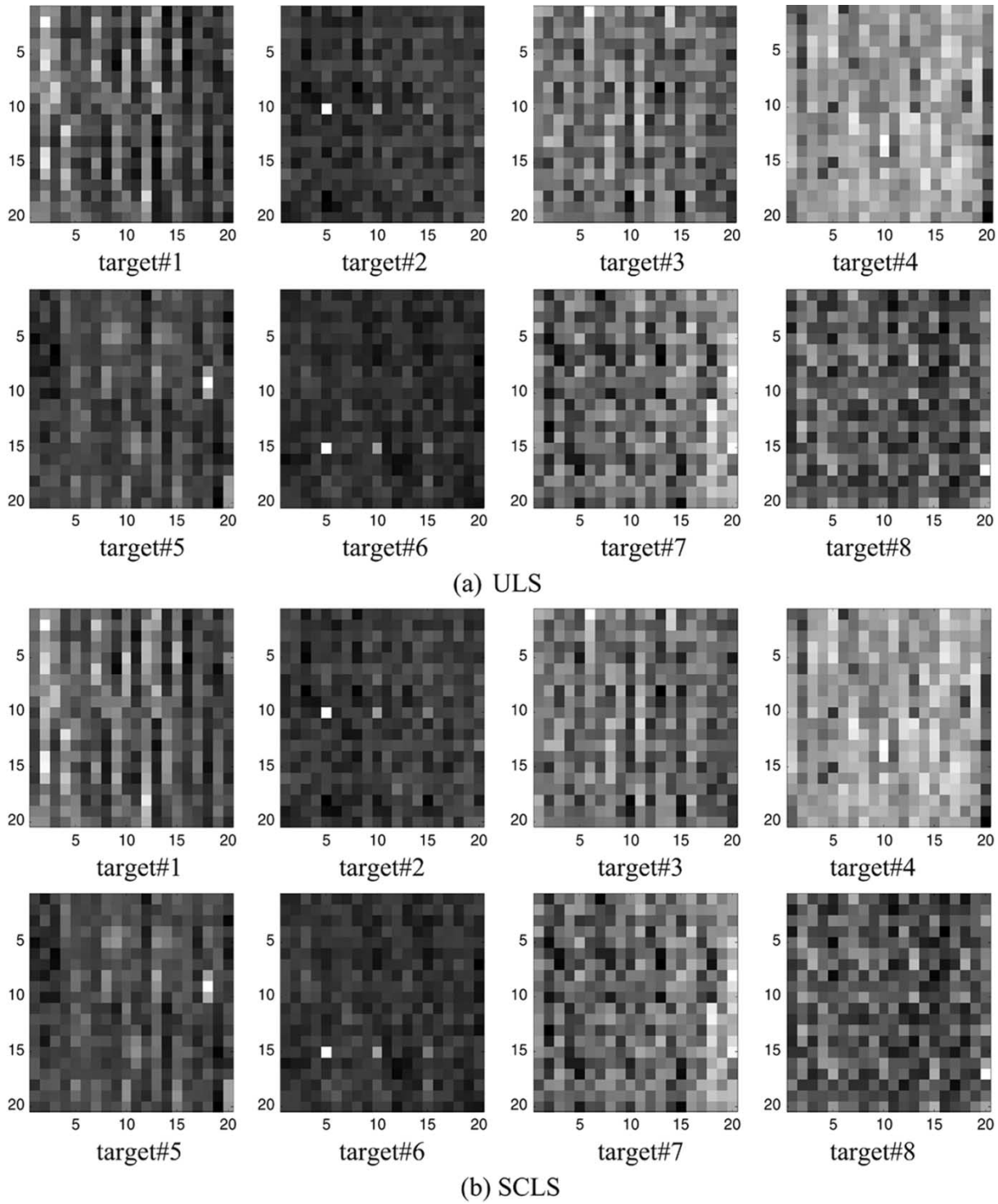

Fig. 7. Detection results of Fig. 4(a) by (a) ULS, (b) SCLS, (c) NCLS, and (d) FCLS.

B. Computer Simulations

In order to substantiate our approach, we simulated a synthetic image scene based on Fig. 1(a) and (b) and the five panel signatures in Fig. 1(c). First of all, 400 grass samples extracted from Fig. 1(a) were used to simulate an image background. Two panel signatures, P1 and P2, were used to simulate two sets of target panels, P_{11}, P_{12}, P_{13} and P_{21}, P_{22}, P_{23}, respectively. The three panels in each set have size ranging from 100%, 50%, and 25% of pixel size (i.e., the ground sampling distance 1.56 m), namely, 2.4336 m^2, 1.2168 m^2, and 0.6084 m^2, respectively. Fig. 2(a) and (b) shows how the target panels P_{12} and P_{13} with size being 50% and 25% of pixel size were simulated. For example, in order to simulate the panel P_{12}, we first simulated two pixel vectors specified by the grass signature and two pixel vectors specified by the panel signature P1 to form a four-pixel square panel where each of four pixel vectors in the panel had size of 2.25 m^2 as shown in Fig. 2(a), and the resulting four-pixel square panel shown in Fig. 2(a) had size of 9 m^2. This four-pixel square panel was then shrunk to 1/4 of its size by averaging all four pixel vectors to reduce the four-pixel square panel with size

of 9 m^2 to a four-pixel square panel with size of 2.25 m^2 as shown in Fig. 2(b) where each pixel vector is only 1/4 of the size of its corresponding pixel vector in Fig. 2(a) as a result of $1/4(\text{P1} + \text{P1} + \text{grass} + \text{grass})$. This shrinking process is similar to the pyramid method developed by Burt and Adelson [11] and illustrated in Fig. 3, where a pixel in an upper layer is obtained by averaging four pixels in its immediate lower layer in a three-layer pyramid. That is, the one pixel at the top layer is the average of the four pixels at the middle layer, whereas a pixel at the middle layer is an average of four pixels at the bottom layer. The shrunk square four-pixel panel in Fig. 2(b) was the desired P_{12}, which contained a subpixel target specified by P1 and with only half size of the pixel. Similarly, P_{13} in Fig. 4(a) was simulated by replacing one "P1" in Fig. 2(a) with a "grass" signature to generate a subpixel target with 25% size of the pixel. Other two subpixel targets $\text{P}_{22}, \text{P}_{23}$ were also generated accordingly in the same way that the two subpixel targets $\text{P}_{12}, \text{P}_{13}$ were generated as just described.

These two sets of the six targets, $\text{P}_{11}, \text{P}_{12}, \text{P}_{13}$ and $\text{P}_{21}, \text{P}_{22}, \text{P}_{23}$, were then implanted in the image background as shown in Fig. 5(a) with the ground truth map of the six implanted target panels shown in Fig. 5(b) where their precise spatial coordinates are specified in the parentheses in $\text{P}_{11}(10, 5), \text{P}_{12}(10, 10), \text{P}_{13}(10, 15)$, $\text{P}_{21}(15, 5), \text{P}_{22}(15, 10), \text{P}_{23}(15, 15)$.

Assume that no prior knowledge is provided for the simulated image scene. So, the exact locations of these six target panels were not supposed to be not known *a priori* and must be found by an unsupervised method. In this case, the ATDCA was used to find these six targets plus other potential targets in the simulated image scene in Fig. 5(a). As a result, eight targets were generated and shown in Fig. 6. They were labeled in accordance with the order that they were found by the ATDCA. In order to see how effective the ATDCA worked, the ground truth map in Fig. 5(b) was used to verify the eight ADTCA-generated targets. It turned out that the pixels labeled 2 and 6 corresponded to panels P_{11} and P_{21}, and the other six targets, numbered 1, 3, 4, 5, 7, and 8 were not panels. One comment is worthwhile, since the ATDCA used the OSP projector $P^{\perp}_{[2,6]}$ to project all the image pixel vectors into the space that was orthogonal to the space linearly spanned by the targets, 2 and 6. As a result, the signatures that were similar to signatures of 2 and 6 were annihilated by $P^{\perp}_{[2,6]}$. The $P^{\perp}_{[2,6]}$-eliminated pixel vectors included the subpixel panels $\text{P}_{12}(10, 10), \text{P}_{13}(10, 15), \text{P}_{22}(15, 10), \text{P}_{23}(15, 15)$ that were specified by signatures of 2 and 6. As a consequence, they were not detected by the ATDCA after the targets 2 and 6 were extracted. As we noted, the six targets 1, 3, 4, 5, 7, and 8 were not panels; they were not annihilated by $P^{\perp}_{[2,6]}$. Therefore, these six targets were detected by the ATDCA subsequently.

Now, we used these eight ATDCA-generated targets as *a posteriori* target information to find other potential targets in the image scene in Fig. 5(a). Four methods were used for this purpose: ULS, SCLS, NCLS, and FCLS. Their respective results are shown in Fig. 7. As we can see, when the detected target 2 was used as the desired target information, the other seven targets (i.e., targets 1, 3, 4, 5, 6, 7, and 8) were considered as undesired targets and were annihilated by the OSP projector. As a result, the second images in Fig. 7(a)–(d) only show the targets specified by the signature of target 2, where all the four methods picked up additional two target panels $\text{P}_{12}, \text{P}_{13}$ whose signatures were similar to the signature of target 2. Similarly, when target 6 was used as the desired target information and the other seven targets (i.e., targets 1, 2, 3, 4, 5, 7, and 8) were considered as undesired targets and annihilated by the OSP projector, all the four methods also pulled out additional two target panels $\text{P}_{22}, \text{P}_{23}$ in the sixth images in Fig. 7(a)–(d). These experiments demonstrated that the ULS, SCLS, NCLS, and FCLS methods could be used for subpixel target detection.

TABLE I
ABUNDANCE FRACTIONS ESTIMATED BY ULS, SCLS. NCLS, AND FCLS

	ULS	SCLS	NCLS	FCLS
P_{11} (1 pixel)	1.0000	1.0000	1.0000	1.0000
P_{12} (50% of pixel)	0.5130	0.4952	0.5142	0.4958
P_{13} (25% of pixel)	0.3387	0.3256	0.3031	0.2908
P_{21} (1 pixel)	1.0000	1.0000	1.0000	1.0000
P_{22} (50% of 1 pixel)	0.5642	0.5814	0.5189	0.4710
P_{23} (25% of 1 pixel)	0.3699	0.3917	0.2877	0.2206

TABLE II
ERROR (PERCENT) RESULTING FROM ULS, SCLS. NCLS, AND FCLS

	ULS	SCLS	NCLS	FCLS
P_{11} (1 pixel)	0.00	0.00	0.00	0.00
P_{12} (1 pixel)	2.60	0.96	2.85	0.83
P_{13} (1 pixel)	35.46	30.22	21.23	16.34
P_{21} (1 pixel)	0.00	0.00	0.00	0.00
P_{22} (1 pixel)	12.85	16.29	3.78	5.80
P_{23} (1 pixel)	47.95	56.70	15.06	11.77

Since our main focus is the size estimation of subpixel targets and only the targets $\text{P}_{11}, \text{P}_{12}, \text{P}_{13}$ and $\text{P}_{21}, \text{P}_{22}, \text{P}_{23}$ had ground truth to validate our results. Therefore, in this paper, only these six P_{11} targets would serve as our interest for the follow-up size estimation. Of course, we could also conduct experiments for the other six found nonpanel targets. Their results could not be used to substantiate our algorithm, due to the lack of ground truth. Because of that, experiments of these six nonpanel targets (1, 3, 4, 5, 7, and 8) were not included in this paper.

In order to see whether the four methods ULS, SCLS, NCLS, and FCLS can further used to estimate size of these panel targets, we calculated the abundance fractions generated by these four methods. Table I tabulates their corresponding results. From Table I, the FCLS yielded the best results, while the NCLS was the second best, but very close to the FCLS. Table II also tabulates the error percentage obtained from Table I by (23), which computes the ratio of the estimation error of target size to the true target size

$$E = 100\% \times \frac{|\text{true size} - \text{estimated size}|}{\text{true size}}. \tag{23}$$

As shown in Table II, the estimated error increases as the target size decreases. When a target fully occupies a pixel, no estimated errors were produced by all the four methods. How-

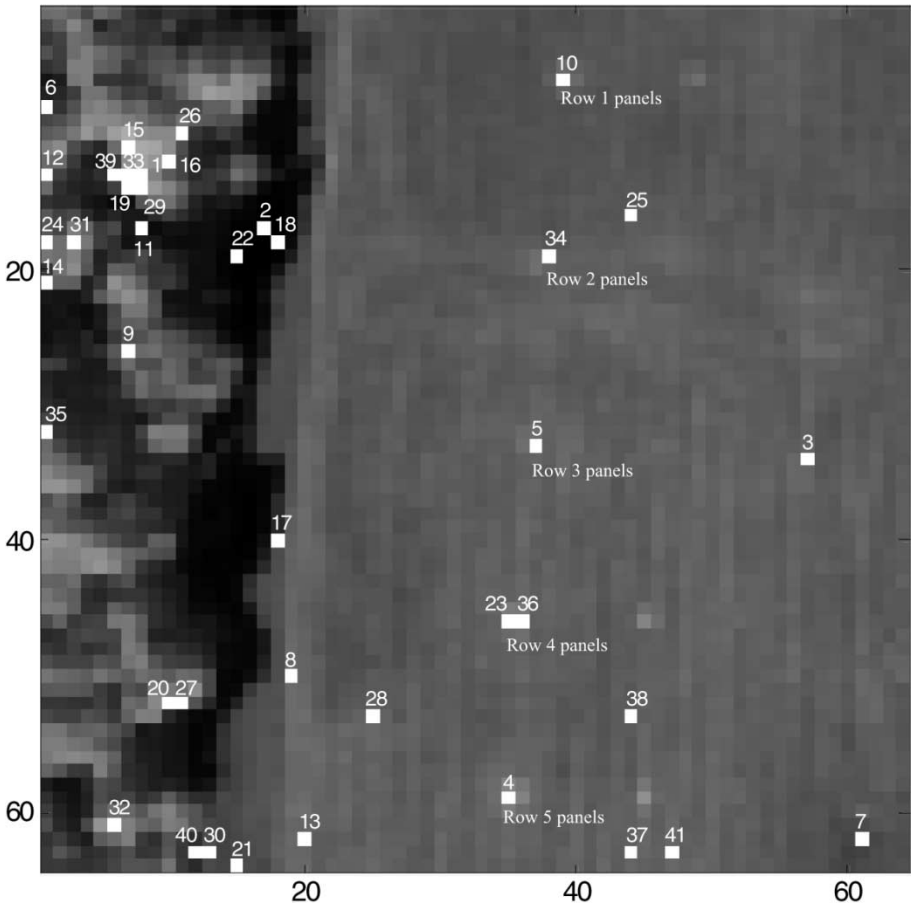

Fig. 8. Forty-one targets detected in the scene of Fig. 1(a) by ATDCA.

ever, when the target size is only 1/4 of a pixel size, the FCLS performed slightly better than the NCLS, but significantly better than the ULS and the SCLS.

These experiments provide evidence that a fully abundance-constrained method is required to achieve better target size estimation when targets are smaller than pixel resolution.

It is worth noting that the ATDCA is an unsupervised method. When it was used, it assumed that no knowledge was provided *a priori*. Consequently, the knowledge of the ATDCA-generated targets remained unknown. In order to identify these target signatures, a database or spectral library is generally required. In our simulations, the ATDCA was implemented with no given prior knowledge. The eight targets extracted by the ATDCA were still unknown. The ground truth of the simulated image in Fig. 5(b) was only used to identify which detected target belonged to the implanted panels so that these targets could be further used to evaluate the effectiveness of subpixel target size estimation. With no ground truth, it is difficult to substantiate our proposed idea. The above computer simulations were conducted to justify its utility.

C. HYDICE Experiments

In this section, the HYDICE image scene in Fig. 1(a) was used for real experiments to further validate the idea proposed in this paper. As noted, the panels $\mathrm{p}_{13}, \mathrm{p}_{23}, \mathrm{p}_{33}, \mathrm{p}_{43}, \mathrm{p}_{53}$ in the third column have spatial resolution of 1 m that is smaller than the pixel size, 1.5 m. These five panels can serve as subpixel targets to test the four methods ULS, SCLS, NCLS, and FCLS. By assuming that no ground truth was provided, the ATDCA was applied to find 41 targets shown in Fig. 8, where the threshold was set to 2.54×10^5, the same threshold used in [4]. These obtained 41 targets were then used as *a posteriori* target information to classify the HYDICE image scene in Fig. 1(a). Now, if we compared these 41 detected targets against the ground truth in Fig. 1(b), we found that the 10th, 34th, 5th, and 4th targets corresponded to $\mathrm{p}_{11}, \mathrm{p}_{21}, \mathrm{p}_{31}$, and p_{51}, respectively. Additionally, both the 23rd and 36th targets detected different pixel vectors in panel p_{41}. Since only these targets had ground truth to verify our results, Fig. 9 only shows the classification results produced by these targets where the classification results in columns (d) and (e) were produced by the two panel pixel vectors in panel p_{41} labeled by the ATDCA-detected 23rd and 36th targets. Apparently, using these six targets, all the four methods have demonstrated different degrees of detecting and classifying the 19 R panel pixel vectors. Table III tabulates the abundance fractions of all the 19 R panel pixel vectors detected by the four methods ULS, SCLS, NCLS, and FCLS. Since both panel pixel vectors in the panel p_{41} were detected by the ATDCA as the 23rd and 36th targets, there are two rows of abundance fractions for each of the three panels in row 4, $\mathrm{p}_{41}, \mathrm{p}_{42}, \mathrm{p}_{43}$ in Table III where the abundance fractions in the first and second rows were detected by using the signatures of the target 23 and target 36 respectively. Interestingly, despite the fact that the ATDCA detected both panel pixel vectors in the panel p_{41}, both target 23 and target 36 were considered as distinct targets. However, only the information of the target 23 could pull out all the three panels in row 4. This phenomenon was evidenced

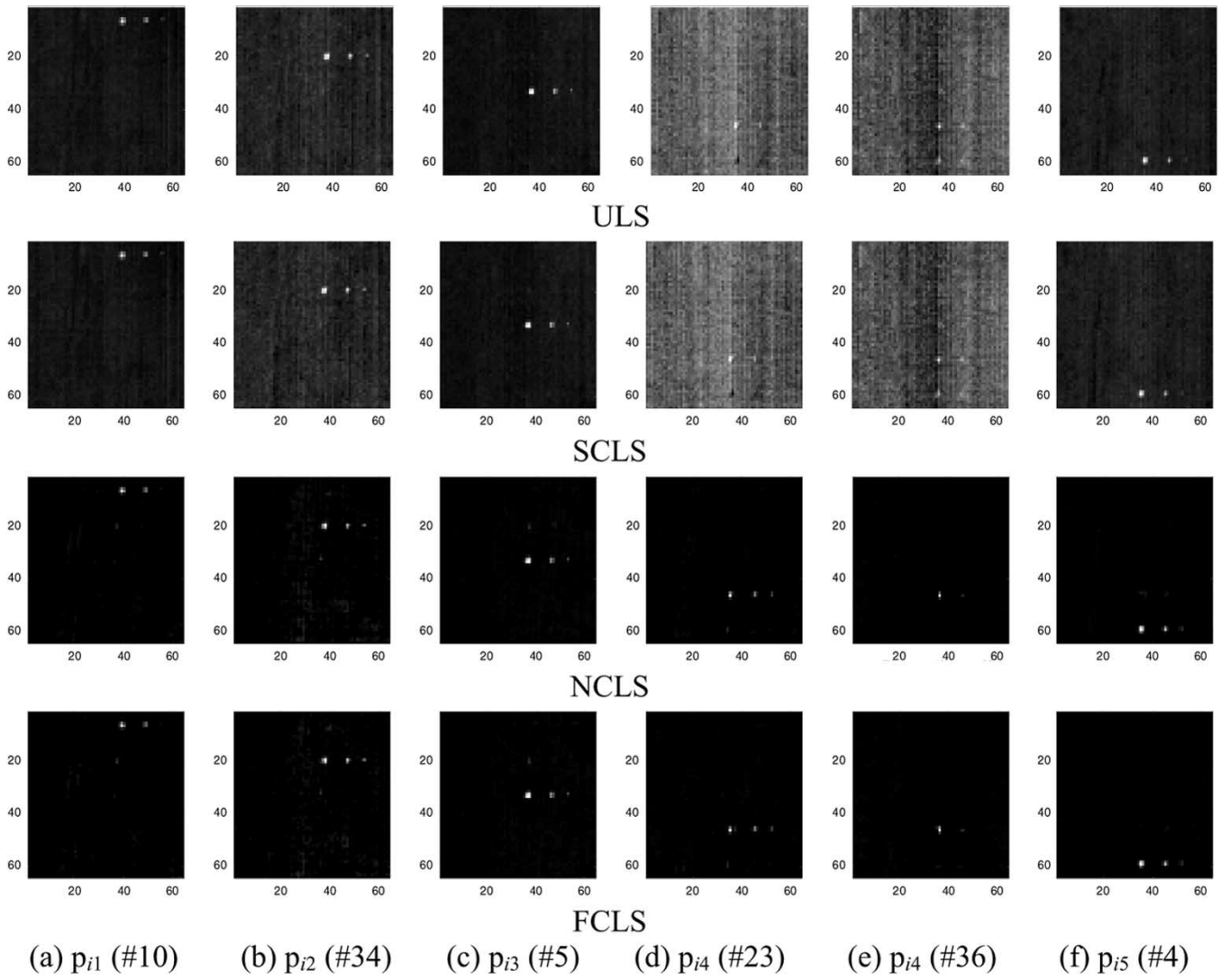

Fig. 9. Abundance fractions of the 15 panels in Fig. 1 estimated by ULS, SCLS. NCLS, and FCLS.

by Table III, where the abundance fractions p_{43} in the second row were detected by the ULS and SCLS using target 36, were negative, and were zeros detected by the NCLS and the FCLS. There are some additional interesting results that can be also observed from Table III. According to the results in Table III, the panel p_{11} was detected as a pure pixel; the panels p_{31} and p_{51} were detected as two-pixel panels, which contained at least one pure pixel; and the panel p_{41} was made up of two pure pixels. The sizes of these four panels estimated by the four methods were very close. The only exception was the panel p_{21}, which was found to be composed of two mixed pixels. As a result, its panel size estimated by the ULS and the SCLS was twice as much as that estimated by the NCLS and the FCLS. It is also interesting to note that the size of all the five targets (10th, 5th, 23rd, 36th, and 4th) found by ATDCA was estimated to be of full pixel size compared to the 34th target, which had an approximate $4/5$ size of a full pixel size. This is because the 34th target pixel detected by the ATDCA was a Y pixel vector, not an R pixel vector like the other five 10th, 5th, 23rd, 36th, and 4th targets. In this case, the 34th target was considered as a mixed-pixel vector, but was detected by the ATDCA as a pure-pixel vector. Consequently, the four methods that used the 34th target produced the two R pixel vectors for the panel p_{21}, which resulted in inaccurate abundance fraction estimates of the R pixels. As an example, Table IV tabulates the FCLS estimated abundance fraction map of all the R and Y pixels that mask the panel p_{21}. As shown in Table IV, the 34th target appeared as a Y pixel vector with its abundance estimated by the FCLS as 1.0000, which indicated that the Y pixel vector was a pure-pixel vector. The two real R pixel vectors next to its left and lined up vertically made up the panel p_{21}. They were estimated by the FCLS as mixed pixels with their corresponding abundance fractions 0.5216 and 0.3455, respectively. This example demonstrated that the ATDCA implemented as an unsupervised method did not always extract pure pixels.

With the ground sampling distance of 1.56 m, the 15 panels with size of 3 m $\times$ 3 m, 2 m $\times$ 2 m, and 1 m $\times$ 1 m shown in Fig. 1 are supposed to occupy three different 3.70, 1.64, and 0.41 pixel sizes, respectively, where an abundance fraction of 1.0 corresponds to one pixel size. Obviously, the abundance fraction estimates of the R pixel vectors in Table III did not provide accurate size estimation for each of the 15 panels. This is because some of the abundance fractions had spread over Y pixel vectors that surround the R pixel vectors. The leakage of such abundance fractions into Y pixel vectors must be included to

TABLE III
ABUNDANCE FRACTIONS OF ALL THE 19 R PANEL PIXEL VECTORS IN THE 15 PANELS ESTIMATED BY ULS, SCLS. NCLS, AND FCLS IN FIG. 9

	ULS	SCLS	NCLS	FCLS
p_{11} (#10)	1.0000	1.0000	1.0000	1.0000
p_{12}	0.4701	0.4634	0.4450	0.4091
p_{13}	0.1190	0.1135	0.0804	0.0496
p_{21} (#34)	0.8144	0.8062	0.5824	0.5216
	0.8273	0.8283	0.4516	0.3455
Total	1.6417	1.6345	1.0340	0.8671
p_{22}	0.7330	0.7701	0.6169	0.6899
p_{23}	0.3218	0.3527	0.3841	0.4177
p_{31}	0.9052	0.9052	0.8640	0.8647
(#5)	1.0000	1.0000	1.0000	1.0000
Total	1.9052	1.9052	1.8640	1.8647
p_{32}	0.5985	0.5985	0.5292	0.5367
p_{33}	0.3997	0.3997	0.3549	0.3614
p_{41} (#23)	1.0000	1.0000	1.0000	1.0000
(#36)	1.0000	1.0000	1.0000	1.0000
Total	2.0000	2.0000	2.0000	2.0000
p_{42}	0.4318	0.4606	0.5464	0.5306
	0.4713	0.4571	0.1616	0.1938
Total	0.9031	0.9177	0.7080	0.7244
p_{43}	0.3966	0.3953	0.2234	0.2543
	-0.0914	-0.0908	0	0
Total	0.3052	0.3045	0.2234	0.2543
p_{51}	0.7216	0.7178	0.7216	0.7217
(#4)	1.0000	1.0000	1.0000	1.0000
Total	1.7216	1.7178	1.7216	1.7217
p_{52}	0.6646	0.6637	0.7801	0.7769
p_{53}	0.1057	0.0959	0.1537	0.1412

TABLE IV
FCLS-ESTIMATED ABUNDANCE FRACTION MAP OF R AND Y PIXEL VECTORS THAT MASK THE PANEL p_{21}

0	0	0.1057	0.2199	0.0846
0.0171	0.1017	0.5216	1.0000	0.1158
0	0.1550	0.3455	0.7520	0.0574
0.0123	0	0	0.0841	0

account for target size estimation. The reason for this inclusion can be best explained by the following example. If we would like to reconstruct a crashed airplane from its debris spread over a wide range of areas, we need to find all the pieces over all locations in order to reassemble the airplane, even though the size of the airplane is relatively small compared to a large coverage of its debris. In light of this interpretation Table IV tabulates the FCLS-estimated abundance fractions of 2 R and 12 Y pixel vectors, where the two R pixel vectors at the center make up the panel p_{21}, and the other 12 Y pixel vectors are their neighboring pixel vectors mixed with the background. According to Table IV, the estimated abundance fractions of the two R pixel vectors were 0.5216 and 0.3455, which indicated that the panel p_{21} was not a pure-pixel vector. So, if only abundance fractions of R pixel vectors were used to estimate the size of the panel p_{21}, its size would be 0.8671 pixel size, which may not

TABLE V
ABUNDANCE FRACTIONS OF ALL THE R AND Y PANEL PIXEL VECTORS IN THE 15 PANELS ESTIMATED BY ULS, SCLS, NCLS, AND FCLS IN FIG. 9

	ULS	SCLS	NCLS	FCLS
p_{11}	3.2094	3.1368	3.1432	3.0329
p_{12}	1.0191	0.9728	1.2892	1.2639
p_{13}	-0.2302	-0.2254	0.0885	0.0496
p_{21}	5.2066	4.9628	3.7033	3.5727
p_{22}	1.2023	1.3001	1.1969	1.4674
p_{23}	0.4698	0.5247	0.5672	0.6148
p_{31}	4.0116	4.0119	4.0922	4.0978
p_{32}	2.5240	2.5239	1.9474	2.0073
p_{33}	0.7715	0.7715	0.4934	0.5144
p_{41}	3.7346	3.7762	3.5161	4.1374
p_{42}	2.6265	2.7857	1.7554	1.9011
p_{43}	0.6861	0.7495	0.5367	0.6132
p_{51}	4.5061	4.5382	3.8530	3.6857
p_{52}	1.5076	1.5119	1.8493	1.8321
p_{53}	0.2772	0.1859	0.4666	0.4604

be accurate. However, if the estimated abundance fractions of 12 Y pixel vectors in Table IV were included in size estimation, the total estimated abundance fractions would be 3.5727, which corresponded to 3.5727 pixel size, and is very close to its true 3.70 pixel size. This simple example suggests that in order to reliably estimate the size of panel targets, we need to include all estimated nonzero abundance fractions that contributed to the panels. This was indeed the case shown in Table V, which tabulates abundance fractions of the R and Y pixel vectors in the 15 panels estimated by ULS, SCLS, NCLS, and FCLS in Fig. 9. Compared to Table III which only computed the estimated abundance fractions of R pixel vectors for target size estimation, Table V produced more accurate results by including the estimated abundance fractions of Y pixel vectors.

VI. CONCLUSION

This paper has presented a new application of constrained linear unmixing to subpixel target size estimation. The proposed idea is to estimate the abundance fraction for a subpixel target present in the image and then uses it to estimate its size. For such an approach to be effective, an accurate estimate of abundance fraction for a subpixel target is required. In this case, a fully constrained abundance linear unmixing is implemented for this purpose. Despite the fact that constrained linear unmixing has been studied extensively for material quantification, the issue investigated in this paper has never been explored in the past. In order to prove our concept, four linear unmixing methods were used for validation, which are an unconstrained linear unmixing method, unconstrained least square, two partially constrained least squares linear unmixing methods, sum-to-one constrained least squares, and nonnegativity constrained least squares, and a fully constrained linear unmixing method, fully constrained least squares. As demonstrated in our simulations and real image experiments, the need of the fully abundance-constrained is evident when the target size is smaller than the ground sampling distance. The target estimation error is increased as the target size is decreased.

ACKNOWLEDGMENT

The first two authors would like to thank support received from the National Research Council and the U.S. Army Edgewood Chemical and Biological Center.

REFERENCES

[1] D. E. Sabol, J. B. Adams, and M. O. Smith, "Quantitative sub-pixel spectral detection in multispectral images," *J. Geophys. Res.*, vol. 97, pp. 2659–2672, 1992.

[2] J. B. Adams, M. O. Smith, and A. R. Gillespie, "Image spectroscopy: Interpretation based on spectral mixture analysis," in *Remote Geochemical Analysis: Elemental and Mineralogical Composition*, C. M. Pieters and P. A. Englert, Eds. Cambridge, U.K.: Cambridge Univ. Press, 1993, pp. 145–166.

[3] J. J. Settle and N. A. Drake, "Linear mixing and estimation of ground cover proportions," *Int. J. Remote Sensing*, vol. 14, pp. 1159–1177, 1993.

[4] D. Heinz and C.-I Chang, "Fully constrained least squares linear mixture analysis for material quantification in hyperspectral imagery," *IEEE Trans. Geosci. Remote Sensing*, vol. 39, pp. 529–545, Mar. 2001.

[5] H. Ren and C.-I Chang, "A generalized orthogonal subspace projection approach to unsupervised multispectral image classification," *IEEE Trans. Geosci. Remote Sensing*, vol. 38, pp. 2515–2528, Nov. 2000.

[6] C.-I Chang, *Hyperspectral Imaging: Techniques for Spectral Detection and Classification*. Amsterdam, The Netherlands: Kluwer, 2003.

[7] H. Ren and C.-I Chang, "Automatic spectral target recognition in hyperspectral imagery," *IEEE Trans. Aerosp. Electron. Syst.*, vol. 39, pp. 1232–1249, Oct. 2003.

[8] C.-I Chang, X. Zhao, M. L. G. Althouse, and J.-J. Pan, "Least squares subspace projection approach to mixed pixel classification in hyperspectral images," *IEEE Trans. Geosci. Remote Sensing*, vol. 36, pp. 898–912, May 1998.

[9] C. L. Lawson and R. J. Hanson, *Solving Least Squares Problems*. Philadelphia, PA: SIAM, 1995.

[10] J. Harsanyi and C.-I Chang, "Hyperspectral image classification and dimensionality reduction: An orthogonal subspace projection approach," *IEEE Trans. Geosci. Remote Sensing*, vol. 32, pp. 779–785, July 1994.

[11] P. J. Burt and E. H. Adelson, "The Laplacian pyramid as a compact image code," *IEEE Trans. Commun.*, vol. 31, pp. 532–540, Apr. 1983.

Chein-I Chang (S'81–M'87–SM'92) received the B.S. degree from Soochow University, Taipei, Taiwan, R.O.C., in 1973, the M.S. degree from the Institute of Mathematics, National Tsing Hua University, Hsinchu, Taiwan, in 1975, and the M.A. degree from the State University of New York, Stony Brook, in 1977, all in mathematics. He received the M.S. and M.S.E.E. degrees from the University of Illinois at Urbana-Champaign in 1982 and the Ph.D. degree in electrical engineering from the University of Maryland, College Park, in 1987.

He has been with the University of Maryland Baltimore County (UMBC), Baltimore, since 1987, as a Visiting Assistant Professor from January 1987 to August 1987, Assistant Professor from 1987 to 1993, Associate Professor from 1993 to 2001, and Professor in the Department of Computer Science and Electrical Engineering since 2001. He was a Visiting Research Specialist in the Institute of Information Engineering at the National Cheng Kung University, Tainan, Taiwan, from 1994 to 1995. He has a patent on automatic pattern recognition and several pending patents on image processing techniques for hyperspectral imaging and detection of microcalcifications. His research interests include automatic target recognition, multispectral/hyperspectral image processing, medical imaging, information theory and coding, signal detection and estimation, and neural networks. He is the author of a book *Hyperspectral Imaging: Techniques for Spectral Detection and Classification* (Norwell, MA: Kluwer). He is on the editorial board and was the Guest Editor of a special issue on telemedicine and applications of the *Journal of High Speed Networks*.

Dr. Chang received a National Research Council Senior Research Associateship Award from 2002 to 2003 at the U.S. Army Soldier and Biological Chemical Command, Edgewood Chemical and Biological Center, Aberdeen Proving Ground, MD. He is an Associate Editor in the area of hyperspectral signal processing for the IEEE TRANSACTIONS ON GEOSCIENCE AND REMOTE SENSING. He is a Fellow of SPIE and a member of Phi Kappa Phi and Eta Kappa Nu.

Hsuan Ren received the B.S. degree in electrical engineering from the National Taiwan University, Taipei, Taiwan, R.O.C., in 1994, and the M.S. and Ph.D. degrees from the University of Maryland Baltimore County, Baltimore, in 1998 and 2000, respectively, all in electrical engineering.

From 2000 to 2003, he received a National Research Council Postdoctor Research Associateship Award supported by the U.S. Army Edgewood Chemical Biological Center. He is currently an Assistant Professor of information engineering with the Center for Space and Remote Sensing, National Central University, Chung-Li, Taiwan, R.O.C. He has two patents pending on hyperspectral target detection and image classification. His research interests include data compression, signal and image processing, and pattern recognition.

Dr. Ren recieved the Third Paper Prize Award in the Student Paper Prize Competition at the IGARSS 2000 Symposium and was one of four finalists in the Student Paper Prize Competition at the IGARSS 1998 Symposium. He is a member of SPIE and Phi Kappa Phi.

Chein-Chi Chang received the B.S. degree from Tamkang University, Taipei, Taiwan, R.O.C., in 1979, the M.S. degree from The Ohio State University, Columbus, in 1981, and the Ph.D. degree in civil engineering from the University of Missouri, Rolla, in 1988.

He has been a Senior Engineer with the District of Columbia Water and Sewer Authority (WASA) since 2000. Prior to joining WASA, he was a licensed Professional Engineer in the State of Maryland and District of Columbia and worked for several engineering consulting companies. He has been an Adjunct Professor with the University of Maryland Baltimore County, the University of Northern Virginia, China Hunan University, and China Central South University. He has been very active in several engineering societies: the American Society of Civil Engineers, the Chinese Institute of Engineers—USA, and the Overseass Chinese Environmental Engineers and Scientists Association. His research interests include multispectral/hyperspectral image processing in environmental applications, system optimization, remote sensing, geographic informations systems, and water resources engineering.

Francis D'Amico, photograph and biography not available at the time of publication.

James O. Jensen, photograph and biography not available at the time of publication.